PAPER IX

# CFD simulations of gas–solid flow in an industrial-scale circulating fluidized bed furnace using subgrid-scale drag models

Particuology 18 (2015) 66–75.

Particuology 18 (2015) 66–75

Contents lists available at ScienceDirect

Particuology

journal homepage: www.elsevier.com/locate/partic

# CFD simulations of gas–solid flow in an industrial-scale circulating fluidized bed furnace using subgrid-scale drag models

Srujal Shah [a,*], Kari Myöhänen [a], Sirpa Kallio [b], Timo Hyppänen [a]

[a] Department of Energy Technology, Lappeenranta University of Technology, FI-53851 Lappeenranta, Finland
[b] VTT Technical Research Centre of Finland, FI-02044 VTT, Finland

ARTICLE INFO

*Article history:*
Received 5 December 2013
Received in revised form 17 April 2014
Accepted 8 May 2014

*Keywords:*
Circulating fluidized bed
Computational fluid dynamics
Two-fluid model
Drag correlation
Modeling

ABSTRACT

Mesoscale flow structures such as clusters and streamers of particles are characteristic features of gas–solid flow in fluidized beds. Numerical simulations of gas–solid flows for industrial-scale fluidized beds are often performed using the Eulerian description of phases. An accurate prediction of this type of flow structure using the Eulerian modeling approach requires a sufficiently fine mesh resolution. Because of the long computational time required when using fine meshes, simulations of industrial-sized units are usually conducted using coarse meshes, which cannot resolve the mesoscale flow structures. This leads to an overestimation of the gas–solid drag force and a false prediction of the flow field. For these cases, a correction must be formulated for the gas–solid drag. We have simulated a large-scale circulating fluidized bed furnace using different gas–solid drag models and compared the model results with measurements.



## Introduction

Because of the advantages of circulating fluidized bed (CFB) combustion technology in the burning of different types of fuel, CFBs have been used extensively in recent decades (Gierse & Leckner, 1996). Efficient modeling tools and reliable experimental data are required to better understanding such multiphase flow systems. The flow in fluidized bed furnaces is complex, and therefore, the accurate simulation of industrial-scale units, which includes hydrodynamics, chemical reactions, and heat transfer, is challenging. An understanding of industrial-scale fluidized bed furnaces is important, and hence, many engineers and researchers have shown an interest in developing methods for their fast and accurate simulation.

Because of significant advancements in high-performance computing facilities, computational fluid dynamics (CFD) is recognized as a promising tool for understanding complex gas–solid flows in fluidized beds. In fluidized beds, the volume fraction of solids can be high (occasionally and locally up to the packing density), and thus, the flow model needs to consider particle–particle interactions. CFD modeling of such flows can be divided into three main categories: (1) Eulerian–Lagrangian collision models, (2) a hybrid Eulerian–Lagrangian approach, such as the multiphase particle-in-cell method, and (3) Eulerian–Eulerian models. The collision models can be classified into a soft- (Tsuji, Kawaguchi, & Tanaka, 1993) and hard-sphere model (Hoomans, Kuipers, Briels, & Van Swaaij, 1996). These models are based on the tracking of individual particles and their collisions. These model approaches have been used to study the small-scale fluidization phenomena, but they cannot be applied to large-scale units because of the associated high computational costs. The multiphase particle-in-cell (MP-PIC) method is based on a Lagrangian tracking of parcels of particles and an Eulerian calculation of the interaction between particles, and between particles and the gas phase (Andrews & O'Rourke, 1996). Although the number of published large-scale studies of this method is small, the MP-PIC method has also been applied to the modeling of combustion reactions (Weng, Nies, & Plackmeyer, 2011). In Ansys Fluent, the available modified MP-PIC method is termed the dense discrete phase model (Adamczyk et al., 2014). Industrial-scale CFD simulations of gas–solid flows in furnaces are typically conducted using the Eulerian description of phases. In the Eulerian–Eulerian two-fluid modeling approach, which is used in this work, both phases are treated as interpenetrating continua (Enwald, Peirano, & Almstedt, 1996; Gidaspow, 1994). Continuity, momentum, and energy equations are solved for both phases. The kinetic theory of granular flow has been used extensively for the closure models of the solid phase momentum equation in the CFD

* Corresponding author. Tel.: +358 401735672.
*E-mail address:* srujal.shah@lut.fi (S. Shah).

http://dx.doi.org/10.1016/j.partic.2014.05.008

**Nomenclature**

| | |
|---|---|
| $C_D$ | particle drag coefficient |
| $d_s$ | solid phase particle diameter, m |
| $e_i$ | restitution coefficient |
| $\vec{g}$ | gravitational acceleration, m/s$^2$ |
| $g_{0,ss}$ | radial distribution function |
| $H_d$ | heterogeneity index |
| $H_i$ | enthalpy, J/kg |
| $h_{sg}$ | volumetric heat transfer coefficient between gas and solid phases, W/(m$^3$ K) |
| $I$ | identity tensor |
| $I_{2D}$ | second invariant of the deviatoric stress tensor |
| $K_{gs}$ | interphase momentum exchange coefficient, kg/(m$^3$ s) |
| $K^*_{gs}$ | interphase momentum exchange coefficient calculated from averaged variables, kg/(m$^3$ s) |
| $k_i$ | thermal phase conductivity, W/(m K) |
| $k_{\Theta_s}$ | diffusion coefficient for granular energy, kg/(m s) |
| $Nu$ | Nusselt number |
| $Pr$ | Prandtl number |
| $p$ | pressure, Pa |
| $Re$ | relative Reynolds number |
| $T_i$ | temperature, K |
| $\vec{v}_i$ | phase velocity, m/s |
| $\tilde{v}_i$ | averaged phase velocity, m/s |

*Greek letters*

| | |
|---|---|
| $\alpha$ | volume fraction |
| $\gamma_{\Theta_s}$ | collisional dissipation of energy, kg/(m s$^3$) |
| $\theta$ | angle of internal friction |
| $\Theta_s$ | granular temperature, m$^2$/s$^2$ |
| $\lambda_i$ | bulk viscosity, Pa s |
| $\mu_i$ | shear viscosity, Pa s |
| $\bar{\bar{\tau}}_i$ | stress–strain tensor, Pa |
| $\varphi_i$ | energy exchange between the gas and solid phases, kg/(m s$^3$) |
| $\omega$ | correction factor |
| $\rho_i$ | density, kg/m$^3$ |

*Subscripts*

| | |
|---|---|
| g | gas |
| i | general index |
| s | solid |

simulations (Benyahia, Arastoopour, Knowlton, & Massah, 2000; Lu, Gidaspow, Bouillard, & Wentie, 2003).

The use of the two-fluid modeling approach with the kinetic theory of granular flow-based closure models requires the calculation mesh to be fine and in the order of a few particle diameters (Andrews, Loezos, & Sundaresan, 2005; Wang, Van der Hoef, & Kuipers, 2009). In a sufficiently fine mesh, mesoscale structures such as clusters and streamers of particles in fluidized beds can be resolved accurately. The two-fluid model with kinetic theory-based closure laws is the preferred approach for small-scale fluidized beds as fine meshes can be still applied. However, for industrial-scale simulations, the requirement of a fine mesh size results in a large number of computational cells. Large-scale simulations with fine meshes are unaffordable, and simulations have to be conducted using coarse meshes. In a coarse mesh simulation, the calculation cell size is larger than the size of meso-scale structures, such as particle clusters. The model assumes a uniform solid concentration within a cell, whereas in reality the flow is non-homogeneous, and the gas flow is able to pass between the small-scale clusters of particles without interaction with the particles. The net gas–solid drag force is therefore increased, which leads to an overestimated solids circulation rate. Therefore, there is a need to formulate a suitable expression for the gas–solid drag, which can be used in CFD simulations of an industrial-scale CFB furnace with a coarse mesh. Similar problems have been encountered with the MP-PIC method (Benyahia & Sundaresan, 2012).

Many research groups have addressed the problem for the formulation of closure models that can be used for coarse mesh simulations (Agrawal, Loezos, Syamlal, & Sundaresan, 2001; Heynderickx, Das, De Wilde, & Marin, 2004; Yang, Wang, Ge, & Li, 2003; Zhang & VanderHeyden, 2002), but in general, a limited number of papers exist in the literature on the simulation of large-scale fluidized beds. One of the reasons for this is the difficulty in obtaining real measurements in commercial units for validating CFD results. The energy-minimization multi-scale (EMMS) approach has been used extensively to formulate a correction factor for the gas–solid drag force. Using the EMMS-based model, a three-dimensional (3D) full-loop industrial-scale CFB has been simulated for one (Zhang, Lu, Wang, & Li, 2010) and also for three solid phases (Lu et al., 2013). A filtering-based approach has also been presented in the literature, in which the results from the fine mesh simulations are filtered to derive constitutive correlations that can be used for coarse mesh simulations (Igci, Andrews, Sundaresan, Pannala, & O'Brien, 2008; Shah, Ritvanen, Hyppänen, & Kallio, 2012). Recently, the filtering-based approach was used to simulate large-scale bubbling and turbulent fluidized beds (Cloete, Johansen, & Amini, 2013). A one-dimensional (1D) model of a steady-state process in a fluidized bed has also been presented in the literature (Matsen, 1982) and has been used as a basis for drag closures in CFD simulations (Kallio, 2005; Vaishali, Roy, & Mills, 2008).

Different parameters have been included in the formulation of a suitable correlation for the correction factor for the gas–solid drag force applicable to coarse mesh-sized simulations. Initially, the correction factor based on the EMMS approach considered only the volume fraction (Yang et al., 2003), but later slip velocity was also included in its formulation (Wang & Li, 2007). For a filtering-based approach, the filter size was the only variable included in the correction factor (Igci et al., 2008), but later, the volume fraction (Igci & Sundaresan, 2011a) and the slip velocity (Milioli, Milioli, Holloway, Agrawal, & Sundaresan, 2013) were also included. Wall effects have also been presented in the literature (Igci & Sundaresan, 2011b; Shah et al., 2012). In addition to the above-mentioned parameters, an effort was made to analyze the effect of material properties, which proved to be important in the formulation of a correction factor for the time-averaged gas–solid drag force (Kallio, Peltola, & Niemi, 2014).

Other terms were also considered in some of the works listed above, such as the stress terms and the correlation between the fluctuations in pressure and the volume fraction. We concentrate on the drag force, which largely determines the concentration of solids at the furnace bottom and top. In the accelerating motion in the lower portion of the furnace above the bottom bed, other terms in the momentum equations can become important, and especially in the equations for the lateral velocity components, Reynolds stress terms can dominate over the drag force. Since no general correlations are available for the subgrid-scale Reynolds stress, we concentrate here on the drag force and evaluate the results of changing the drag force model only.

Various research groups have published several CFD simulations comparing different drag model closures, but most of their studies focus on small-scale apparatus. In this work, a commercial-scale CFB unit is used and a coarse mesh is applied, which provides a better basis for the comparison of different subgrid-scale models

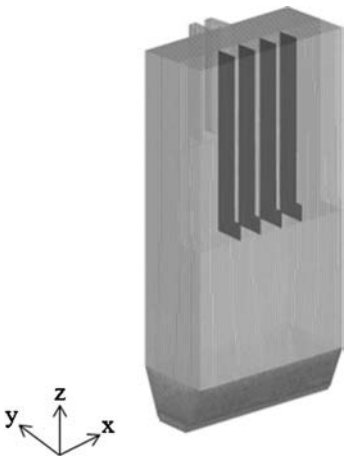


**Fig. 1.** Domain of the simulated CFB furnace.

for practical calculations. The same CFB unit was considered in our earlier paper (Shah, Myöhänen, Klajny, & Hyppänen, 2013), but in that work, a comparison was made only between the homogenous and space-averaged drag models. In this paper, different correlations of the correction factor for the drag model are presented as a function of volume fraction. The correlations are then applied to simulate an industrial-scale circulating fluidized bed furnace. CFD simulations with the corrected forms of the drag model are performed and compared with the homogeneous drag model.

## Simulation methodology

### *Geometry and model description*

The domain of the study is the large-scale CFB furnace, which was modeled earlier by Shah, Klajny, Myöhänen, and Hyppänen (2009). The model domain is presented in Fig. 1. The height of the furnace is ~43 m and the cross-section is 14.3 m × 6.73 m. The cell dimensions were ~0.1–0.3 m, and the number of calculation cells was ~400,000. Hexahedral and tetrahedral cells were used for most of the domain and for the tapered lower furnace section, respectively.

The model boundaries included the primary air through the grate, the secondary air through multiple secondary air nozzles and other ports, and the solid fed from the solid circulation ports. The inlet values as well as the measured pressure profile data were based on the test balance measurements by the boiler manufacturer, and the data were the same as in the earlier study by Shah et al. (2009). In large-scale CFD simulations of CFB furnaces, the reactions are often ignored and the furnace is assumed to be isothermal (e.g. Zhang et al., 2010). This is acceptable because the proportion of the gas flow because of reactions is relatively small and the temperature profile in a CFB furnace is fairly uniform. In this case, the estimated total additional gas flow because of the reactions would have been ~7% of the total inlet air flow, and thus it would not have any significant effect on the results.

A major exception to the isothermal-assumption is the temperature of the inlet gases, which is much lower than the furnace temperature. If the mass flow of the inlet gas is set correctly and the inlet temperature is set to the furnace temperature, the velocity of the gas jet, for example, at the tip of the secondary air nozzle, would be much higher than in reality, and thus the model would not simulate the real conditions. In our approach, the inlet gas temperatures were set according to the measurements (490 K), and the temperature of the solids was set to a fixed value (1150 K), which was based on the measured average furnace temperature. The heat transfer between the hot solids and the gas was included in the model to better simulate the expansion of cold inlet gases as they penetrate the furnace.

**Table 1**
Cumulative distribution of different particle sizes in the furnace.

| Particle size (μm) | 62.5 | 125 | 180 | 500 | 2000 | 6000 |
|---|---|---|---|---|---|---|
| Cumulative share (%) | 2.9 | 40.7 | 59.7 | 84.4 | 94.8 | 100 |

In our earlier study by Shah et al. (2009), the bed material was simulated as a mixture of two solid phases with a fine and a coarse particle size (128 and 1500 μm). The higher solid concentration at the bottom of the furnace was thus achieved with the presence of the coarse solid phase. In this study, the modeling was attempted with a single solid phase with a particle diameter of 155 μm, which corresponds with the measured average particle size of the bed. In such industrial-scale furnaces, solids have a particle size distribution, and the selection of a single particle size in the simulations is not straightforward, and can affect the results. Moreover, it is questionable whether it is possible to simulate such a system with only one particle size. However, calculations limited to one solid phase are often applied in large-scale studies to reduce the computational effort. Table 1 shows the cumulative particle size distribution in the furnace to provide a better idea of the particle size chosen in the CFD simulations. Based on the pressure profile measurements, the total bed inventory was approximately 50,000 kg, which was controlled in the model by adjusting the feed rate from the return leg chutes.

### *CFD simulations*

CFD simulations of the gas–solid flow were performed using the commercial code, Ansys Fluent 13, by applying a two-fluid model and by using the kinetic theory of granular flow. The governing equations and the closure models are given in Table 2.

Simulations were performed for different cases and were allowed to reach stable-state conditions in which the outlet mass flow rate appears to be stable. An averaging of the result data was performed over 30 s of simulation time. A first order implicit discretization scheme was used for time-stepping and a first order upwind discretization scheme was used for the other terms. A second order upwind discretization was attempted, but it led to convergence problems. The phase-coupled SIMPLE algorithm was used for pressure–velocity coupling. The number of iterations per time step was set to 10. With these settings, the residual behavior showed an acceptable numerical convergence, and the relative error between two successive iterations for each scaled residual component was below $1 \times 10^{-3}$. The gas phase turbulence model was not used in this study and the flow was modeled as laminar flow. At the walls, a free slip boundary condition was used for the gas phase and the partial slip boundary conditions of the Johnson and Jackson (1987) model with a specularity coefficient of 0.001 and particle-wall restitution coefficient of 0.2 were used for the solid phase. The properties for the CFD simulations as used in Ansys Fluent are given in Table 3.

All the CFD simulation cases presented in this work were performed for the same set of model equations and boundary conditions, except for the correlation for the interphase momentum exchange coefficient in the drag force model, which was changed for different cases. The first one is the homogeneous drag law with the correlation proposed by Gidaspow, Bezburuah, and Ding

**Table 2**
Governing equations and closure models used.

Gas phase (continuity, momentum, and energy equations)

$$\frac{\partial}{\partial t}(\alpha_g \rho_g) + \nabla \cdot (\alpha_g \rho_g \vec{v}_g) = 0$$

$$\frac{\partial}{\partial t}(\alpha_g \rho_g \vec{v}_g) + \nabla \cdot (\alpha_g \rho_g \vec{v}_g \vec{v}_g) = -\alpha_g \nabla p + \nabla \cdot \bar{\bar{\tau}}_g + \alpha_g \rho_g \vec{g} + K_{gs}(\vec{v}_s - \vec{v}_g)$$

$$\frac{\partial}{\partial t}(\alpha_g \rho_g H_g) + \nabla \cdot (\alpha_g \rho_g \vec{v}_g H_g) = \nabla \cdot (k_g \nabla T_g) + h_{sg}(T_g - T_s)$$

Solid phase (continuity, momentum, and energy equations)

$$\frac{\partial}{\partial t}(\alpha_s \rho_s) + \nabla \cdot (\alpha_s \rho_s \vec{v}_s) = 0$$

$$\frac{\partial}{\partial t}(\alpha_s \rho_s \vec{v}_s) + \nabla \cdot (\alpha_s \rho_s \vec{v}_s \vec{v}_s) = -\alpha_s \nabla p - \nabla p_s + \nabla \cdot \bar{\bar{\tau}}_s + \alpha_s \rho_s \vec{g} + K_{gs}(\vec{v}_g - \vec{v}_s)$$

$$\frac{\partial}{\partial t}(\alpha_s \rho_s H_s) + \nabla \cdot (\alpha_s \rho_s \vec{v}_s H_s) = \nabla \cdot (k_s \nabla T_s) + h_{sg}(T_s - T_g)$$

Granular energy equation

$$\frac{3}{2}\left[\frac{\partial}{\partial t}(\alpha_s \rho_s \Theta_s) + \nabla \cdot (\alpha_s \rho_s \vec{v}_s \Theta_s)\right] = (-p_s \bar{\bar{I}} + \bar{\bar{\tau}}_s) : \nabla \vec{v}_s + \nabla \cdot (k_{\Theta_s} \nabla \Theta_s) - \gamma_{\Theta_s} + \varphi_{gs}$$

Diffusion coefficient for granular energy

$$k_{\Theta_s} = \frac{15 d_s \rho_s \alpha_s \sqrt{\pi \Theta_s}}{4(41-33\eta)}\left[1 + \frac{12}{5}\eta^2(4-3\eta)\alpha_s g_{0,ss} + \frac{16}{15}(41-33\eta)\eta\alpha_s g_{0,ss}\right], \text{ where } \eta = \frac{1}{2}(1+e_{ss})$$

Collisional dissipation of energy

$$\gamma_{\Theta_s} = \frac{12(1-e_{ss}^2)g_{0,ss}}{d_s\sqrt{\pi}} \rho_s \alpha_s^2 \Theta_s^{3/2}$$

Energy exchange between the gas and solid phases

$$\varphi_{gs} = -3K_{gs}\Theta_s$$

Phase stress-strain tensors

$$\bar{\bar{\tau}}_g = \alpha_g \mu_g (\nabla \vec{v}_g + \nabla \vec{v}_g^T) - \frac{2}{3}\alpha_g \mu_g \nabla \cdot \vec{v}_g \bar{\bar{I}}$$

$$\bar{\bar{\tau}}_s = \alpha_s \mu_s (\nabla \vec{v}_s + \nabla \vec{v}_s^T) + \alpha_s \left(\lambda_s - \frac{2}{3}\mu_s\right) \nabla \cdot \vec{v}_s \bar{\bar{I}}$$

Solids shear viscosity

$$\mu_s = \mu_{s,col} + \mu_{s,kin} + \mu_{s,fr}$$

$$= \frac{4}{5}\alpha_s \rho_s d_s g_{0,ss}(1+e_{ss})\left(\frac{\Theta_s}{\pi}\right)^{1/2} + \frac{\alpha_s \rho_s d_s \sqrt{\Theta_s \pi}}{6(3-e_{ss})}\left[1 + \frac{2}{5}(1+e_{ss})(3e_{ss}-1)\alpha_s g_{0,ss}\right] + \frac{p_s \sin\theta}{2\sqrt{I_{2D}}}$$

Granular bulk viscosity

$$\lambda_s = \frac{4}{3}\alpha_s \rho_s d_s g_{0,ss}(1+e_{ss})\left(\frac{\Theta_s}{\pi}\right)^{1/2}$$

Solids pressure

$$p_s = \alpha_s \rho_s \Theta_s + 2\rho_s(1+e_{ss})\alpha_s^2 g_{0,ss}\Theta_s$$

Radial distribution function

$$g_{0,ss} = \left[1 - \left(\frac{\alpha_s}{\alpha_{s,\max}}\right)^{1/3}\right]^{-1}$$

Volumetric heat transfer coefficient between gas and solid phases

$$h_{sg} = \frac{6k_g \alpha_g \alpha_s \mathrm{Nu}}{d_s^2}, \text{ where } \mathrm{Nu} = (7 - 10\alpha_g + 5\alpha_g^2)(1 + 0.7Re^{0.2}Pr^{1/3}) + (1.33 - 2.4\alpha_g + 1.2\alpha_g^2)Re^{0.2}Pr^{1/3}$$

(1992), which is a combination of the Wen and Yu (1966) model and the Ergun (1952) equation model. The other three cases considered the effect of subgrid-scale modeling. Four calculations with different drag models were performed: Model A with the drag law of the Ergun/Wen–Yu model, Model B with the space-averaged drag model, Model C with the EMMS drag model, and Model D with the macroscopic drag model as described in the following section.

## Drag model correlations

The role of the interphase drag model in the CFD simulations is very important as it is one of the main parameters that characterize the behavior of the gas–solid flow in fluidized beds. In the gas and solid phase momentum equations, the drag force term is expressed as the product of the interphase momentum exchange coefficient and the slip velocity. Several correlations are available in the literature for the interphase momentum exchange coefficient. The form of the drag force correlation for a homogeneous suspension is either formulated from the experimental data (Ergun, 1952; Wen & Yu, 1966) or from numerically accurate Lattice-Boltzmann simulations (Hill, Koch, & Ladd, 2001; Hill, Koch, & Ladd, 2001; Van der Hoef, Beetstra, & Kuipers, 2005). For heterogeneous conditions, the approaches to derive drag laws are based on measurements, fine-mesh simulation, and/or theoretical considerations. We have implemented different drag models to analyze their effect on the overall gas–solid flow behavior. The comparison of the used drag models is given as a function of gas volume fraction in Fig. 2. A brief description of the used drag model correlations is presented below and its mathematical expressions are given in Table 4.

**Table 3**
Properties for CFD simulations in Ansys Fluent.

| | |
|---|---|
| Gas phase | Incompressible ideal gas<br>Molar mass = 28.872 kg/kmol<br>$\mu = 4.37 \times 10^{-5}$ Pa s |
| Solid phase | Diameter = 155 μm<br>Density = 2500 kg/m$^3$ |
| Restitution coefficient | 0.9 |
| Maximum packing limit | 0.63 |
| Mesh size (m) | 0.1–0.3 |
| Time step size (s) | 0.001 |

It has become common practice in the literature to use the notation of the heterogeneity index, $H_d$. This notation was first introduced for the EMMS model to compare the hydrodynamic disparity between homogeneous and heterogeneous fluidization (Wang & Li, 2007). In later studies, this notation has been used to compare the different drag correlations, and it is termed the scaling factor for the drag coefficient (Igci & Sundaresan, 2011a) or the function accounting for unresolved structures (Schneiderbauer, Puttinger, & Pirker, 2013). In all of these studies, $H_d$ is defined as the ratio of the different drag correlations to the Wen–Yu drag model. Fig. 3 compares the heterogeneity index of the different drag models used in this work as a function of gas volume fraction.

*Drag model A: Ergun/Wen–Yu model*

The Ergun/Wen–Yu model is a combination of the Wen–Yu drag model and the drag model based on the Ergun equation. The combination of these two models is termed the Gidaspow or homogeneous drag model. The model was presented such that, at higher gas volume fractions, the Wen–Yu model would be used, and for

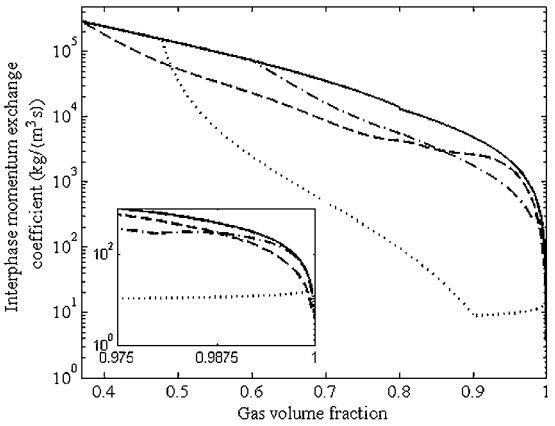


**Fig. 2.** Comparison of interphase momentum exchange coefficients using different models. The value of slip velocity is taken as unity. The solid, dashed, dash-dotted, and dotted lines represent the Ergun/Wen–Yu drag model, space-averaged drag model, drag from the EMMS model, and macroscopic drag model, respectively. The inset figure is used to visualize the curves more clearly at higher gas volume fraction values.

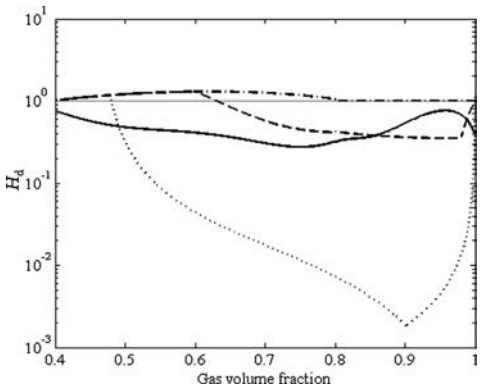


**Fig. 3.** Comparison of heterogeneity indices, $H_d$, for different drag models versus gas volume fraction. The value of slip velocity is taken as unity. ($H_d = 1$ is for the Wen–Yu drag model, the dash-dotted, solid, dashed, and dotted lines represent the Ergun/Wen–Yu drag model, the space-averaged drag model, the drag from the EMMS model, and the macroscopic drag model, respectively.)

lower gas volume fractions, the Ergun equation model would be used. Despite the discontinuity of the model at 0.8, it is commonly used in the fluidization literature.

*Drag model B: space-averaged model*

It is well known that CFD simulations using the two-fluid model are dependent on mesh size. Thus, a macroscopic set of equations must be formulated for coarse mesh simulations. In this approach, the space-averaging method was used to derive the subgrid-scale

**Table 4**
Drag model correlations used in CFD simulations.

Drag model A: Ergun/Wen–Yu model

When $\alpha_g > 0.8$,

$$K_{gs} = \frac{3}{4} C_D \frac{\alpha_s \alpha_g \rho_g |\vec{v}_s - \vec{v}_g|}{d_s} \alpha_g^{-2.65},$$

where $C_D = \frac{24}{\alpha_g Re}[1 + 0.15(\alpha_g Re)^{0.687}]$ and $Re = \frac{\rho_g d_s |\vec{v}_s - \vec{v}_g|}{\mu_g}$;

When $\alpha_g \le 0.8$,

$$K_{gs} = 150 \frac{\alpha_s (1-\alpha_g)\mu_g}{\alpha_g d_s^2} + 1.75 \frac{\alpha_s \rho_g |\vec{v}_s - \vec{v}_g|}{d_s}.$$

Drag model B: space-averaged model

When $\alpha_g > 0.8$,

$$K_{gs} = \frac{3}{4} C_D \frac{\alpha_s \alpha_g \rho_g |\vec{v}_s - \vec{v}_g|}{d_s} \alpha_g^{-2.65} \omega_{WY},$$

where $\omega_{WY} = -4055.2\alpha_g^4 + 14124\alpha_g^3 - 18404\alpha_g^2 + 10636\alpha_g - 2300.4$;

When $\alpha_g \le 0.8$,

$$K_{gs} = \omega_E \left( 150 \frac{\alpha_s (1-\alpha_g)\mu_g}{\alpha_g d_s^2} + 1.75 \frac{\alpha_s \rho_g |\vec{v}_s - \vec{v}_g|}{d_s} \right),$$

where $\omega_E = 162.52\alpha_g^4 - 401.57\alpha_g^3 + 370.53\alpha_g^2 - 152.01\alpha_g + 23.809$.

Drag model C: EMMS model

When $\alpha_g > 0.60$,

$$K_{gs} = \frac{3}{4} C_D \frac{\alpha_s \alpha_g \rho_g |\vec{v}_s - \vec{v}_g|}{d_s} \omega_{EMMS},$$

where $\omega_{EMMS} = \begin{cases} 30.739\alpha_g - 29.739, & \alpha_g > 0.98 \\ 124.77\alpha_g^4 - 474.59\alpha_g^3 + 681.97\alpha_g^2 - 439.94\alpha_g + 108.15, & 0.80 < \alpha_g \le 0.98 \\ 1449.2\alpha_g^4 - 4692.4\alpha_g^3 + 5722.4\alpha_g^2 - 3117.2\alpha_g + 641.1, & 0.60 < \alpha_g \le 0.80 \end{cases}$;

When $\alpha_g \le 0.60$,

$$K_{gs} = 150 \frac{\alpha_s (1-\alpha_g)\mu_g}{\alpha_g d_s^2} + 1.75 \frac{\alpha_s \rho_g |\vec{v}_s - \vec{v}_g|}{d_s}.$$

Drag model D: macroscopic model

When $\alpha_g > 0.478$,

$$K_{gs} = \frac{3}{4} C_D \frac{\alpha_s \alpha_g \rho_g |\vec{v}_s - \vec{v}_g|}{d_s} \omega_M^{-2},$$

where $\omega_M = \begin{cases} 1, & \alpha_g > 0.9996 \\ 73.42(1-\alpha_g)^{0.5565}, & 0.901 < \alpha_g \le 0.9996 \\ 4.062 \frac{\alpha_g - 0.46}{\alpha_s \alpha_g} + \frac{0.022}{\alpha_g}, & 0.478 < \alpha_g \le 0.901 \end{cases}$;

When $\alpha_g \le 0.478$,

$$K_{gs} = 150 \frac{\alpha_s (1-\alpha_g)\mu_g}{\alpha_g d_s^2} + 1.75 \frac{\alpha_s \rho_g |\vec{v}_s - \vec{v}_g|}{d_s}.$$

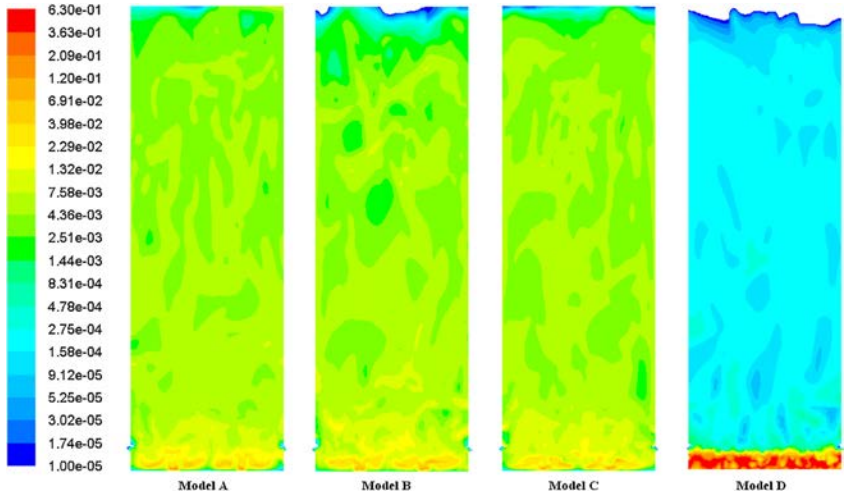


**Fig. 4.** Instantaneous solid volume fraction contours for different drag models used at $y = 3.365$ m. The value of solid volume fraction less than $1 \times 10^{-5}$ on a logarithmic scale is colorless. (Models A, B, C, and D represent the Ergun/Wen–Yu, the space-averaged, the EMMS, and the macroscopic model, respectively.)

model for the gas–solid drag force. The fine mesh results of the vertical component of the drag force are averaged, and a correction coefficient is then written as a function of the averaged variables as shown in mathematical notation:

$$^{\Delta x}\left\langle {}^{\delta x}_{\delta t}(K_{gs}(v_{g,z} - v_{s,z}))\right\rangle = \omega K^{*}_{gs}(\tilde{v}_{g,z} - \tilde{v}_{s,z}), \quad (1)$$

where $\omega$ is the correction factor to be modeled, $\delta t$ is the time step, $\delta x$ is the fine mesh size, $\Delta x$ is the coarse mesh size, $K_{gs}$ is the interphase momentum exchange coefficient, $K^{*}_{gs}$ is the interphase momentum exchange coefficient calculated from the averaged variables (Ergun/Wen–Yu model), $v_{g,z}$ and $v_{s,z}$ are the phase velocities, and $\tilde{v}_{g,z}$ and $\tilde{v}_{s,z}$ are the averaged phase velocities. We have used the same data that was generated for the previous article (Shah et al., 2012), based on the fine mesh two-dimensional (2D) simulation of the CFB riser. The principle follows that the results obtained from the fine mesh simulation with mesh size $\delta x$ are averaged over the coarse averaging size $\Delta x$.

In the study by Shah et al. (2012), different averaging sizes up to 0.05 m were used, and lower correction factor values resulted as the averaging size increased. In this study, the maximum cell size is 0.3 m. Thus, even the values produced with the largest averaging size (0.05 m) may not produce small enough values of $\omega$ for this case. Using an averaging size of 0.05 m, the data generated by Shah et al. (2012) was applied to determine the correction factor as a function of the gas volume fraction. In the 2D study (Shah et al., 2012), the correction factor is affected by the distance from the wall and the slip velocity, but for this study, these effects were neglected and a correction factor was set as a function of the volume fraction only.

*Drag model C: EMMS model*

The EMMS model was presented in detail by Li et al. (1999), who describe the heterogeneous flow structure of a circulating fluidized bed system. The main parameter to describe the heterogeneity is the formation of clusters. According to the EMMS approach, gas and particles are considered to be in a dense or a dilute phase, and the mechanisms of the gas–solid interaction are analyzed at different scales. The set of structure parameters such as voidages and velocities is described for both dilute and dense phases resulting in a non-linear set of equations. The interphase momentum exchange coefficient is related implicitly to the structure parameters. In similar work for simulating large-scale furnaces using the EMMS model (Lu et al., 2013; Zhang et al., 2010), a correction factor was formulated as a function of slip velocity and volume fraction, and it predicted the overall fluidized bed behavior successfully. We use the correction factor of the interphase momentum exchange coefficient as a function of volume fraction only.

The correction factor for the EMMS model was generated using EMMS software obtained from the Institute of Process Engineering, Chinese Academy of Sciences. The parameters that were used to generate the correction function are given in Table 3 with a superficial fluidization velocity of 2.66 m/s and a solids flux of 5 kg/(m$^2$ s) corresponding to the boiler considered in this study. The superficial velocity changes along the furnace height, but fortunately the EMMS method is not very sensitive to changes in this parameter and the same correction function can be used for the whole furnace.

*Drag model D: macroscopic model*

The drag model described in this section is the correlation presented originally by Matsen (1982). It considers the ratio of the average slip velocity to the terminal velocity of a particle. Poikolainen (1992) used this model in a 1D analysis, and Kallio (2005) and Vaishali et al. (2008) used it as a basis for drag closure in CFD modeling. In the Matsen (1982) model, the slip velocity is approximated as the terminal velocity of a particle for very dilute suspensions. It increases as the solid concentration increases, indicating the formation of clusters. For dense phase suspensions, an equation is applied based on the bubbling theory of two-phase flows. Fig. 3 shows that the combination of these two models leads to very low values and an abrupt change in the heterogeneity index, which is not fully realistic. Matsen (1982) presented model parameters for a case of Geldart group A particles. To use the model for other conditions and Geldart group B particles, the model parameters need to be changed. In the work of the transient simulations of a CFB riser, Kallio (2005) used similar equations as formulated by Matsen (1982) and Poikolainen (1992), with the modification

that close to the packing limit, the drag force is calculated from the Ergun equation. This equation set is shown in Table 4. We consider the same type of equation set as is used by Kallio (2005). Kallio (2005) used the data for Geldart group B particles in two different cases, in addition to Matsen's parameters, to express the model parameters as functions of the Archimedes number. We have used the same expressions to calculate the coefficients for the model on the basis of material property values for the boiler considered.

The formulated equations, which were used as a basis for the above equations, were for the time-averaged description. Moreover, Matsen's correlations were based on a 1D analysis of fluidization conditions, which leads to a small overestimation of the drag correction when used locally in 2D and 3D modeling. We applied the same formulation for the drag force for the 3D transient simulation of a case that consists of a very coarse mesh applicable to industrial-scale furnaces. It can be expected that even though the mesh size is very coarse, the macroscopic steady-state drag model used here can be considered to be an extreme correction compared with the actually required value. A significant amount of temporal variations of solids velocities and voidages is produced by the transient coarse mesh simulation, leading to an overestimation of the drag correction when the steady-state, macroscopic drag model is applied. Because the macroscopic model provides the absolute limit for a coarse mesh drag closure, it is useful as a comparison and is therefore included.

## Results and discussion

### *Solid volume fraction*

The solid volume fraction is an important parameter in gas–solid flows. Fig. 4 shows the instantaneous solid volume fraction contours for different drag models used in this study. The subgrid-scale models, such as the space-averaged and EMMS models, produce similar solids distributions as the Ergun/Wen–Yu model. The macroscopic model predicts a very dense solids concentration in the lower part of the furnace and a very dilute region in the upper part of the furnace.

Fig. 5(a) compares the time-averaged simulation results for different drag models with the pressure measurements. The profiles from the simulations are plotted against the height where the measurements were taken. The pressure predicted using the Ergun/Wen–Yu model is excessively high throughout the riser height. The pressure is reduced when the space-averaged and EMMS models are used, but the results still do not match the measurements accurately. It should be noted that the modeled pressure profiles could have been adjusted to better match the measurements simply by increasing the particle size that was used in the model. However, the main purpose of this study was to compare the different model approaches when using measurement-based data. Hence, this type of sensitivity analysis was not performed. The pressure profile predicted using the macroscopic drag model is reduced significantly in the lower part of the furnace whereas in the upper part, the pressure is mainly uniform. Fig. 5(b) presents the behavior of different drag models compared with the measurements by studying the pressure gradient divided by density and gravity. In the experimental work, the solid concentration is often determined in this manner from the pressure gradient. The Ergun/Wen–Yu model predicts the lower and higher values at the bottom and upper part of the furnace, respectively. A slight improvement results when subgrid-scale drag models, such as the space-averaged and EMMS models, are used, especially in the top region, but these models do not predict accurate values. When the macroscopic model is used, an overestimated correction to the drag force results. A very dense lower and a dilute middle and upper region are predicted by using the macroscopic model.

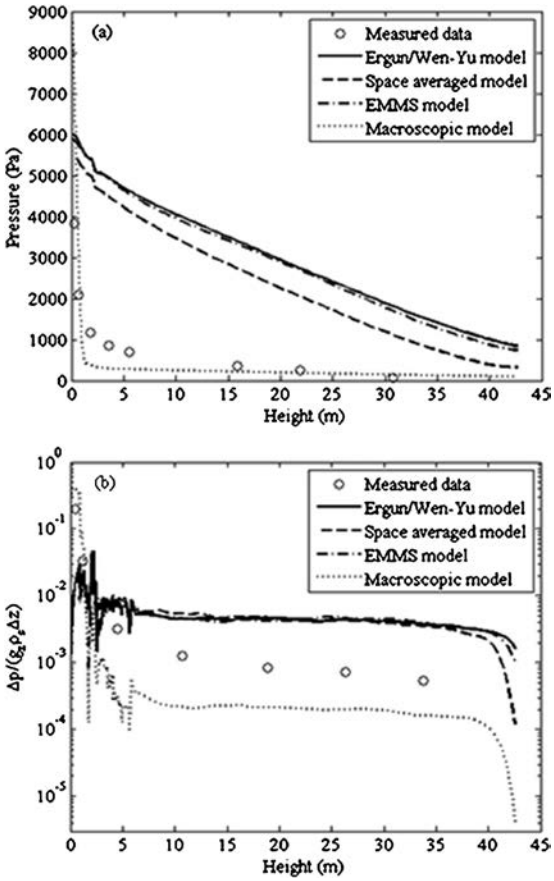


**Fig. 5.** Comparison of simulation results for different drag models versus furnace height with measurements for (a) pressure and (b) pressure gradient divided by density and gravity.

### *Solid vertical velocity*

The solid velocity is also an important variable that describes how solids move in the furnace. Fig. 6 shows the Favre-averaged solids vertical velocity at different furnace heights. The profiles are plotted at the centerline of the furnace at a depth of 3.365 m. The profiles are not smooth, possibly because of the duration of the averaging time (30 s). In general, an averaging time of a few minutes would make more sense, but this was not done because of the excessive computational time requirements. The solids velocity remains mainly positive when the Ergun/Wen–Yu model is used. With the use of subgrid-scale drag models, such as the space-averaged, EMMS, and macroscopic models, a clear upflow of solids is observed at the central region and downflow occurs near the walls. This type of flow structure has often been measured in industrial-scale CFB units (Werther, 2005).

Similar profiles were plotted along the depth direction as shown in Fig. 7. The profiles are smoother in the depth direction compared

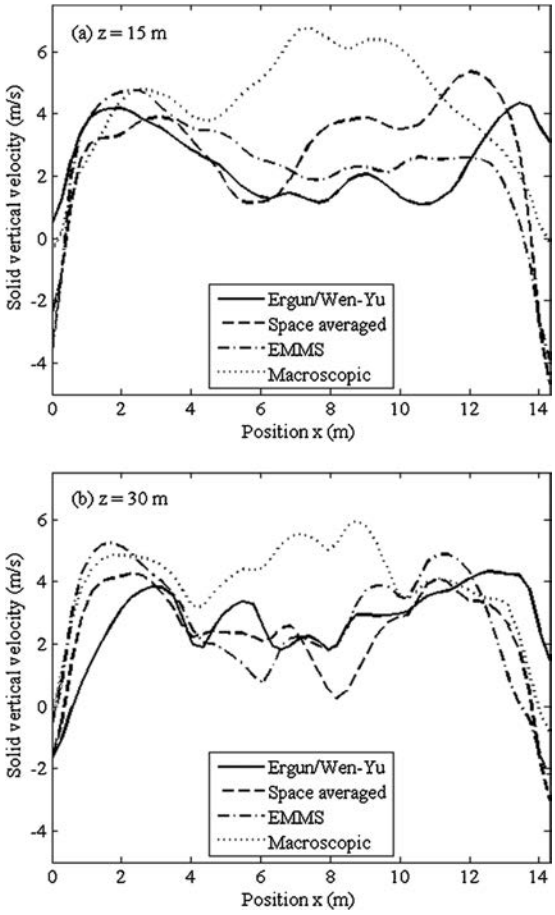


**Fig. 6.** Favre-averaged solid vertical velocity at different furnace heights: (a) $z = 15$ m and (b) $z = 30$ m. The results are plotted along the width direction of the furnace.

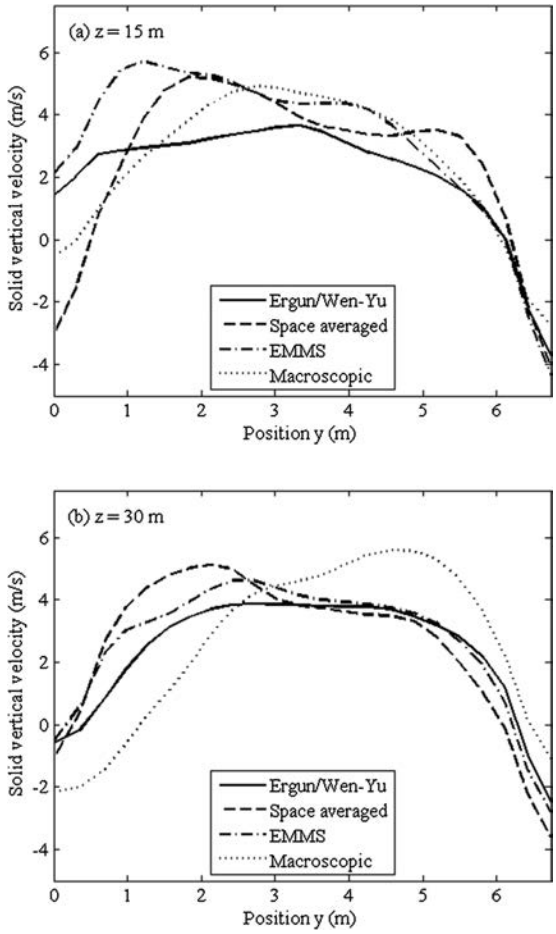


**Fig. 7.** Favre-averaged solid vertical velocity at two different furnace heights (a) $z = 15$ m and (b) $z = 30$ m. The results are plotted along the depth direction of the furnace.

with the width direction, because of the arrangement of feed and solid circulation ports at the bottom of the furnace, which affect the profiles in the width direction. The profiles are plotted at 3 m from the left side-wall of the furnace. Furthermore, across this direction, the solids have a higher velocity at the center and lower velocities near the walls. The velocity profiles show a down-flow of solids near the back wall for all the drag models.

*Solids mass flow*

An accurate prediction of solids mass flow is crucial in gas–solid flow simulations. The transient data of the solids mass flow rate at the furnace outlet has been computed and is shown in Fig. 8 for different drag models during the last 30 s of the simulations. Unfortunately, the modeled mass flows cannot be compared with the measurements because of technical difficulties related to determining the circulating mass flow in a commercial CFB.

As observed from Fig. 8, the highest solids mass flow rate is obtained using the Ergun/Wen–Yu model. With the other drag models, as expected, a decrease in the mass flow rate occurs at the outlet. The EMMS model predicts only a slightly lower mass flow rate compared with the Ergun/Wen–Yu model. It should be noted that the EMMS model also overpredicts the solids flux as the mesh size used in the simulations is coarse (Lu, Wang, & Li, 2009). The space-averaged drag model was formulated using a smaller averaging size. It can be expected that an even larger correction is needed when a coarse mesh is used, as is done in this work. Also, the formulation was conducted for 2D studies, and the resulting correlation was applied to 3D simulations. The predicted mass flow rate using the macroscopic model is very low compared with the other models.

Fig. 9 shows the averaged vertical solids mass flux profiles at different furnace heights. The profiles are plotted at the centerline of the furnace for the value in the depth direction at 3.365 m. The Ergun/Wen–Yu model predicts that the solids flux is mainly positive. With the use of subgrid-scale drag models, such as the space-averaged and EMMS models, a clear upflow of solids can be seen at the central region and a downflow of solids occurs near the walls. Using the macroscopic model, the flux is almost zero across the width direction when plotted on this scale. The predicted solids

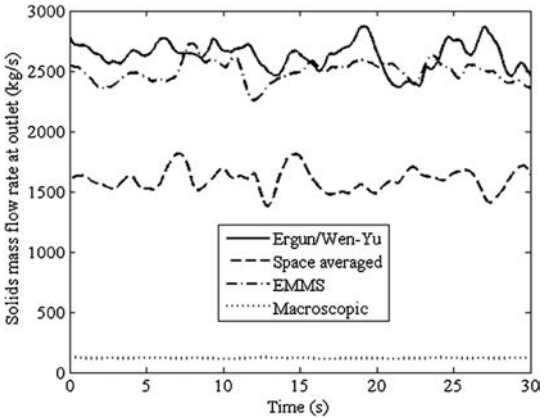


**Fig. 8.** Variations of solids mass flow rates with time at the outlet using different drag models.

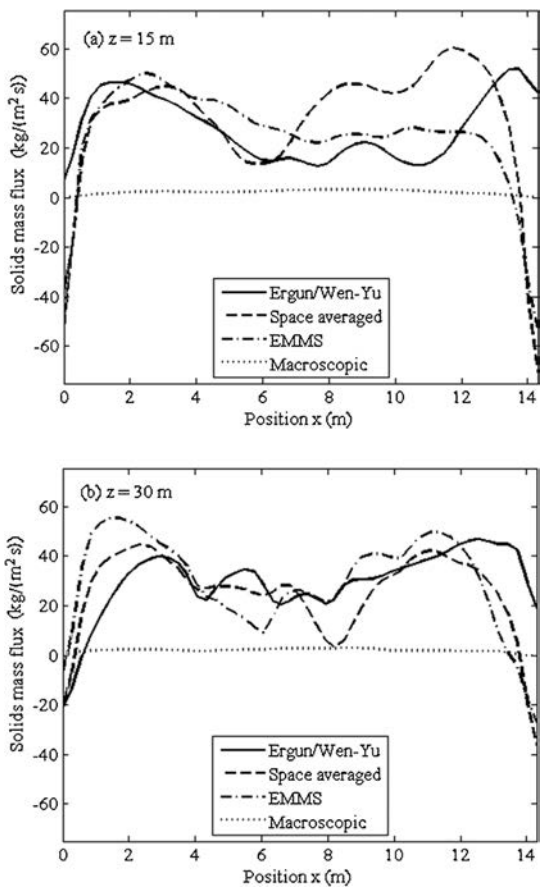


**Fig. 9.** Averaged vertical solids mass flux profiles along the width direction at two different furnace heights: (a) $z = 15$ m and (b) $z = 30$ m.

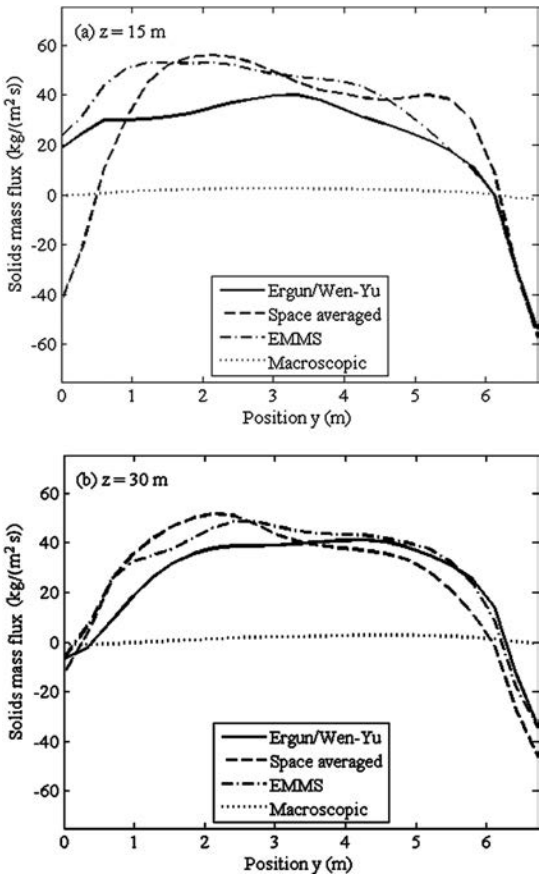


**Fig. 10.** Averaged vertical solids mass flux profiles along the depth direction at two different furnace heights: (a) $z = 15$ m and (b) $z = 30$ m.

concentration is low in the upper region of the furnace when it is calculated using the macroscopic model, and this explains the small flux in Fig. 9.

Fig. 10 shows the averaged vertical solids mass flux for different furnace heights in the depth direction. The profiles are plotted at 3 m from the left side-wall of the furnace. Similar profiles can be seen as for the width direction as described in Fig. 9. A clear down-flow of solids can be seen near the walls, especially at the back wall.

## Conclusions

CFD simulations of an industrial-scale circulating fluidized bed furnace were performed using the Eulerian model. Different subgrid-scale drag models were applied and compared with the Ergun/Wen–Yu model. All the subgrid-scale models showed better predictions compared with the Ergun/Wen–Yu model. Although a large difference exists between the measured and predicted vertical solids distribution in the riser, the model simulates the core-annulus flow structure correctly, with qualitatively realistic down- and upflow velocities. The subgrid-scale models were based on correcting the interphase momentum exchange coefficient as

a function of volume fraction only. It is likely that other factors, such as the slip velocity, distance from the wall, material properties, and the filter size, should be included in the correction models. As an upper limit for the subgrid-scale drag model, a macroscopic model designed for steady-state simulations was also tested for comparison. As expected, the macroscopic model produced a significantly strong effect. The required correction to the drag force in very coarse meshes was found to lie between the drag corrections produced by the models in the literature and those required in steady-state modeling.

Nonetheless, more research is required in this area, particularly in the accurate matching of solids concentration profiles with measurement data and computations with coarse meshes. It should be emphasized that the simulations presented in this study were performed for one solid particle diameter, whereas solids have a wide particle size distribution in large-scale furnaces. This will be the scope of our future research work.

## Acknowledgements

The authors would like to express their gratitude to Prof. Wei Wang at the Institute of Process Engineering, Chinese Academy of Sciences, for fruitful discussions and for providing assistance with the EMMS software. The authors acknowledge Foster Wheeler Energia Oy for providing the measurement data for comparison with the simulation results.

## References

Adamczyk, W. P., Węcel, G., Klajny, M., Kozołub, P., Klimanek, A., & Białecki, R. A. (2014). Modeling of particle transport and combustion phenomena in a large-scale circulating fluidized bed boiler using a hybrid Euler–Lagrange approach. *Particuology*, http://dx.doi.org/10.1016/j.partic.2013.10.007

Agrawal, K., Loezos, P. N., Syamlal, M., & Sundaresan, S. (2001). The role of mesoscale structures in rapid gas–solid flows. *Journal of Fluid Mechanics*, *445*, 151–185.

Andrews IV, A. T., Loezos, P. N., & Sundaresan, S. (2005). Coarse-grid simulation of gas-particle flows in vertical risers. *Industrial & Engineering Chemistry Research*, *44*, 6022–6037.

Andrews, M. J., & O'Rourke, P. J. (1996). The multiphase particle-in-cell (MP-PIC) method for dense particulate flows. *International Journal of Multiphase Flow*, *22*, 379–402.

Benyahia, S., Arastoopour, H., Knowlton, T. M., & Massah, H. (2000). Simulation of particles and gas flow behavior in the riser section of a circulating fluidized bed using the kinetic theory approach for the particulate phase. *Powder Technology*, *112*, 24–33.

Benyahia, S., & Sundaresan, S. (2012). Do we need sub-grid scale corrections for both continuum and discrete gas-particle flow models? *Powder Technology*, *220*, 2–6.

Cloete, S., Johansen, S. T., & Amini, S. (2013). Evaluation of a filtered model for the simulation of large scale bubbling and turbulent fluidized beds. *Powder Technology*, *235*, 91–102.

Enwald, H., Peirano, E., & Almstedt, A. E. (1996). Eulerian two-phase flow theory applied to fluidization. *International Journal of Multiphase Flow*, *22*, 21–66.

Ergun, S. (1952). Fluid flow through packed columns. *Chemical Engineering Progress*, *48*, 89–94.

Gidaspow, D. (1994). *Multiphase flow and fluidization: Continuum and kinetic theory descriptions*. San Diego: Academic Press.

Gidaspow, D., Bezburuah, R., & Ding, J. (1992). Hydrodynamics of circulating fluidized beds: Kinetic theory approach. In O. E. Potter, & D. J. Nicklin (Eds.), *Proceedings of the 7th engineering foundation conference on fluidization* (pp. 75–82). New York: Engineering Foundation.

Gierse, M., & Leckner, B. (1996). Operation control of circulating fluidized bed boilers. *International Journal of Energy Research*, *20*, 839–851.

Heynderickx, G. J., Das, A. K., De Wilde, J., & Marin, G. B. (2004). Effect of clustering on gas–solid drag in dilute two-phase flow. *Industrial & Engineering Chemistry Research*, *43*, 4635–4646.

Hill, R. J., Koch, D. L., & Ladd, A. J. C. (2001a). Moderate-Reynolds-number flows in ordered and random arrays of spheres. *Journal of Fluid Mechanics*, *448*, 243–278.

Hill, R. J., Koch, D. L., & Ladd, A. J. C. (2001b). The first effects of fluid inertia on flows in ordered and random arrays of spheres. *Journal of Fluid Mechanics*, *448*, 213–241.

Hoomans, B. P. B., Kuipers, J. A. M., Briels, W. J., & Van Swaaij, W. P. M. (1996). Discrete particle simulation of bubble and slug formation in a two-dimensional gas-fluidised bed: A hard-sphere approach. *Chemical Engineering Science*, *51*, 99–118.

Igci, Y., Andrews IV, A. T., Sundaresan, S., Pannala, S., & O'Brien, T. (2008). Filtered two-fluid models for fluidized gas–particle suspensions. *AIChE Journal*, *54*, 1431–1448.

Igci, Y., & Sundaresan, S. (2011a). Constitutive models for filtered two-fluid models of fluidized gas-particle flows. *Industrial & Engineering Chemistry Research*, *50*, 13190–13201.

Igci, Y., & Sundaresan, S. (2011b). Verification of filtered two-fluid models for gas-particle flows in risers. *AIChE Journal*, *57*, 2691–2707.

Johnson, P. C., & Jackson, R. (1987). Frictional-collisional constitutive relations for granular materials, with application to plane shearing. *Journal of Fluid Mechanics*, *176*, 67–93.

Kallio, S. (2005). Comparison of simulated and measured voidage and velocity profiles and fluctuations in a CFB riser. In K. Cen (Ed.), *Proceedings of the 8th International conference on circulating fluidized beds* (pp. 105–112). Beijing: International Academic Publishers.

Kallio, S., Peltola, J., & Niemi, T. (2014). Parametric study of the time-averaged gas–solid drag force in circulating fluidized bed conditions. *Powder Technology*, *257*, 20–29.

Li, J., Cheng, C., Zhang, Z., Yuan, J., Nemet, A., & Fett, F. N. (1999). The EMMS model—Its application, development and updated concepts. *Chemical Engineering Science*, *54*, 5409–5425.

Lu, B., Wang, W., & Li, J. (2009). Searching for a mesh-independent sub-grid model for CFD simulation of gas–solid riser flows. *Chemical Engineering Science*, *64*, 3437–3447.

Lu, B., Zhang, N., Wang, W., Li, J., Chiu, J. H., & Kang, S. G. (2013). 3-D full-loop simulation of an industrial-scale circulating fluidized-bed boiler. *AIChE Journal*, *59*, 1108–1117.

Lu, H. L., Gidaspow, D., Bouillard, J., & Wentie, L. (2003). Hydrodynamic simulation of gas–solid flow in a riser using kinetic theory of granular flow. *Chemical Engineering Journal*, *95*, 1–13.

Matsen, J. M. (1982). Mechanisms of choking and entrainment. *Powder Technology*, *32*, 21–33.

Milioli, C. C., Milioli, F. E., Holloway, W., Agrawal, K., & Sundaresan, S. (2013). Filtered two-fluid models of fluidized gas-particle flows: New constitutive relations. *AIChE Journal*, *59*, 3265–3275.

Poikolainen, V. (1992). *Mathematical modeling of gas–solid fluidization with a one-dimensional hydrodynamical model* Master thesis. Finland: Lappeenranta University of Technology (in Finnish).

Schneiderbauer, S., Puttinger, S., & Pirker, S. (2013). Comparative analysis of subgrid drag modifications for dense gas–particle flows in bubbling fluidized beds. *AIChE Journal*, *59*, 4077–4099.

Shah, S., Klajny, M., Myöhänen, K., & Hyppänen, T. (2009). Improvement of CFD methods for modeling full scale circulating fluidized bed combustion systems. In G. Yue, H. Zhang, C. Zhao, & Z. Luo (Eds.), *Proceedings of the 20th international conference on fluidized bed combustion* (pp. 792–798). Beijing: Tsinghua University Press.

Shah, S., Myöhänen, K., Klajny, M., & Hyppänen, T. (2013). Numerical modeling of gas–solids flow in large scale circulating fluidized bed using subgrid-scale model. In J. A. M. Kuipers, R. F. Mudde, J. R. van Ommen, & N. G. Deen (Eds.), *Proceedings of the fluidization XIV* (pp. 575–582). New York: Engineering Conferences International.

Shah, S., Ritvanen, J., Hyppänen, T., & Kallio, S. (2012). Space averaging on a gas–solid drag model for numerical simulations of a CFB riser. *Powder Technology*, *218*, 131–139.

Tsuji, Y., Kawaguchi, T., & Tanaka, T. (1993). Discrete particle simulation of two-dimensional fluidized bed. *Powder Technology*, *77*, 79–87.

Vaishali, S., Roy, S., & Mills, P. L. (2008). Hydrodynamic simulation of gas–solids downflow reactors. *Chemical Engineering Science*, *63*, 5107–5119.

Van der Hoef, M. A., Beetstra, R., & Kuipers, J. A. M. (2005). Lattice–Boltzmann simulations of low-Reynolds-number flow past mono- and bidisperse arrays of spheres: Results for the permeability and drag force. *Journal of Fluid Mechanics*, *528*, 233–254.

Wang, W., & Li, J. (2007). Simulation of gas–solid two-phase flow by a multi-scale CFD approach—Extension of the EMMS model to the sub-grid level. *Chemical Engineering Science*, *62*, 208–231.

Wang, J., Van der Hoef, M. A., & Kuipers, J. A. M. (2009). Why the two-fluid model fails to predict the bed expansion characteristics of Geldart A particles in gas-fluidized beds: A tentative answer. *Chemical Engineering Science*, *64*, 622–625.

Wen, C. Y., & Yu, Y. H. (1966). Mechanics of fluidization. *Chemical Engineering Progress Symposium Series*, *62*, 100–111.

Weng, M., Nies, M., & Plackmeyer, J. (2011). Computer-aided optimisation of the gas–particle flow and combustion at the Duisburg circulating fluidised bed furnace. *VGB PowerTech Journal*, *91*(8), 64–69.

Werther, J. (2005). Fluid dynamics, temperature and concentration fields in large scale CFB combustors. In K. Cen (Ed.), *Proceedings of the 8th international conference on circulating fluidized beds* (pp. 1–25). Beijing: International Academic Publishers.

Yang, N., Wang, W., Ge, W., & Li, J. (2003). CFD simulation of concurrent-up gas–solid flow in circulating fluidized beds with structure-dependent drag coefficient. *Chemical Engineering Journal*, *96*, 71–80.

Zhang, D. Z., & VanderHeyden, W. B. (2002). The effects of mesoscale structures on the macroscopic momentum equations for two-phase flows. *International Journal of Multiphase Flow*, *28*, 805–822.

Zhang, N., Lu, B., Wang, W., & Li, J. (2010). 3D CFD simulation of hydrodynamics of a 150 $MW_e$ circulating fluidized bed boiler. *Chemical Engineering Journal*, *162*, 821–828.